Thermal CO_2 Sorption / Reaction on Perovskite-Type Oxide Ceramics

Takumi Watanabe*, Yuping Xu*, Yunzi Xin*, Takashi Shirai*, **

*Advanced Ceramics Research Center, Nagoya Institute of Technology, Gokiso-cho, Showa-ku, Nagoya, Aichi 466-8555, JAPAN

**Department of Life Science and Applied Chemistry, Graduate School of Engineering, Nagoya Institute of Technology, Gokiso-cho, Showa-ku, Nagoya, Aichi 466-8555, JAPAN

Abstract:

This review summarizes recent advancements in the thermal capture and conversion of carbon dioxide (CO_2) using perovskite-type oxide ceramics. We focus on the structural flexibility and defect engineering of ABO_3 oxides, particularly the unique CO_2 sorption characteristics of nanostructured $BaTiO_3$ derived from its high surface-to-volume ratio and intense surface potential fields. The discussion extends to CO_2 conversion pathways, such as the reverse water-gas shift (RWGS) reaction and hydrocarbon production pathways, facilitated by the Mars-van Krevelen-like mechanism over lattice oxygen vacancies. Furthermore, we highlight an innovative approach for the direct low-temperature decomposition of CO_2 into solid carbon using nanoparticles, which utilizes a pseudo-high-pressure state within confined nanopores. Overall, this work demonstrates how controlling nanostructures and surface chemical environments provides a strategic framework for high-efficiency carbon management.

1. Introduction

Anthropogenic emissions of carbon dioxide (CO_2) have increased dramatically since the industrial revolution and are widely recognized as the primary cause of contemporary climate change, leading to ocean acidification, global warming, land desertification, and sea-level rise.[1] Global CO_2 emissions reached a record 36.3 Gt in 2024, marking a 0.9% year-on-year increase. This persistent upward trend is rapidly exhausting the remaining carbon budget, with current projections indicating that the 1.5 ℃ warming threshold may be surpassed within five years, if it has not been exceeded already.[2, 3] As reported, the concentration of CO_2 in the atmosphere has soared from 340 to 408 ppm between 1980 and 2019,[4] and it is anticipated to rise to 950 ppm by the end of the 21st century. Therefore, it is vital to mitigate CO_2 emissions.[5] These trends highlight the urgent need to reduce greenhouse gas emissions and develop technologies for CO_2 mitigation and utilization.

The IPCC Sixth Assessment Report (AR6) provides a comprehensive global evaluation of climate change mitigation pathways, establishing rigorous benchmarks for limiting global warming to 1.5 ℃. According to the AR6, to maintain this temperature threshold with no or limited overshoot, global greenhouse gas (GHG) emissions must peak before 2025 and be reduced by approximately 43% by 2030 relative to 2019 levels. Furthermore, the report states that achieving the 1.5 ℃ target necessitates reaching net-zero CO_2 emissions globally by the early 2050s, followed by net-zero GHG emissions in the second half of the century. These authoritative findings underscore the requirement for a rapid and deep transition across all sectors, characterized by a substantial decline in the use of unabated fossil fuels and the accelerated deployment of low-carbon technologies. This global framework set by the AR6 serves as the primary scientific basis for current international climate policy and the urgent development of innovative CO_2 utilization strategies.[6, 7]

Various approaches have been proposed for CO_2 management, including carbon capture and storage (CCS) and carbon capture and utilization (CCU), as illustrated in Figure 1. In CCU strategies, CO_2 is treated not only as a waste product but also as a potential carbon resource that can be converted into value-added chemicals or fuels.[8] Representative examples include catalytic hydrogenation reactions such as methanation (Sabatier) and the reverse water–gas shift (RWGS) reaction, as well as electrochemical and photocatalytic CO_2 reduction. Despite significant progress in these areas, CO_2 is a thermodynamically very stable molecule, and its decomposition requires a large amount of energy: the energies required for C=O bond dissociation ($CO_2 \rightarrow CO + O$), dissociation into carbon and oxygen ($CO_2 \rightarrow C + O_2$), and atomization ($CO_2 \rightarrow C + 2O$) are 526.1, 1104, and 1598 kJ mol^{-1}, respectively.[9] Thermodynamic calculation reveals that ΔG becomes negative above 3075 ℃ for the reaction of $2CO_2 = 2CO + O_2$ (Figure

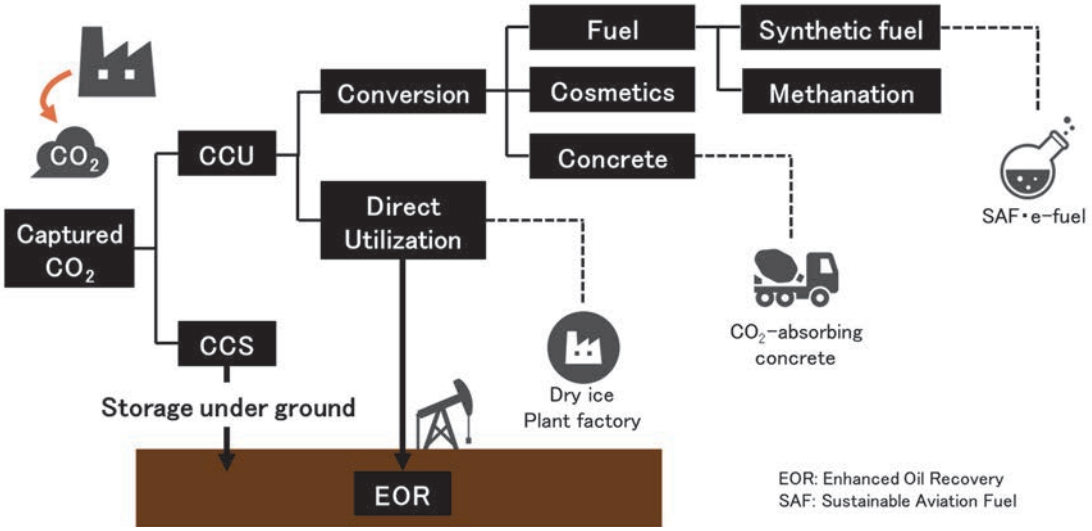

Figure 1. Conceptual diagram of CCU and CCS.

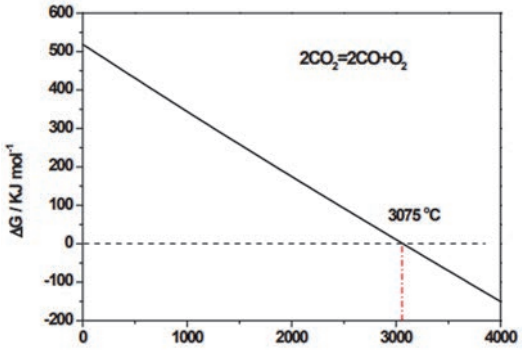

Figure 2. Temperature variations of ΔG for direct CO_2 splitting at 1 bar. Reprinted from ref. [10]. Copyright © 2017 Royal Society of Chemistry.

2).[10] Thus, the high activation energy required for C–O bond cleavage remain major challenges for efficient catalytic conversion.

Metal oxides have long been investigated as catalysts for CO_2-related reactions because of their thermal stability, tunable electronic structures, and rich defect chemistry. Among them, perovskite-type oxides (ABO_3) have attracted considerable attention due to their structural flexibility[11, 12] and the ability to control oxygen vacancy concentrations through cation substitution or reduction treatments.[13-16] These properties enable perovskite oxides to participate in redox reactions involving lattice oxygen and have led to their use in applications such as gas sensing,[17-19] catalysis,[20-24] and thermochemical energy conversion.[25, 26]

Recent studies have also suggested that perovskite oxides can potentially interact strongly with CO_2 molecules through surface sorption processes. In particular, ferroelectric perovskites such as $BaTiO_3$ exhibit spontaneous surface polarization and charge redistribution, which may influence the adsorption and activation of gas molecules.[27-31] Furthermore, nanostructuring of perovskite oxides significantly increases surface area and defect density, potentially enhancing CO_2 adsorption and catalytic activity.[32-38]

In addition to CO_2 sorption, perovskite oxides have been investigated as catalysts for CO_2 conversion reactions. Conventional approaches typically require reducing agents such as hydrogen to drive reactions including methanation,[39] the RWGS reaction,[40] and the other routes.[41] Basically, in these reactions, two-step redox chemical looping involving oxygen vacancies in metal oxides are utilized for CO_2 splitting with/without external reducing gases. However, such thermochemical cycles usually require very high operating temperatures at 1000-1600 K for reduction part.[10, 42, 43]

More recently, nanoscale perovskite oxides have been reported to promote CO_2 decomposition under comparatively mild conditions. In particular, nanoscale $BaTiO_3$ ceramics have demonstrated unique behavior, including strong CO_2 sorption and low-temperature thermolysis leading to the formation of carbon materials.[33, 44] These observations suggest that nanostructuring and defect engineering of perovskite oxides may open new pathways for CO_2 activation and conversion.

In this review, we summarize recent progress in thermal CO_2 sorption and reaction on perovskite-type oxide ceramics. First, the interaction mechanisms between CO_2 molecules with perovskite oxide surfaces and its performance are discussed. Next, catalytic conversion of CO_2 on perovskite oxides is described, including reactions with reducing gases as well as CO_2 decomposition processes without external reductants,

highlighting recent advances in low-temperature CO_2 thermolysis on nanoscale ABO_3 materials.

2. CO_2 sorption on Perovskite-type oxides

Understanding the interaction between CO_2 molecules and oxide surfaces is essential for designing materials capable of efficient CO_2 capture and conversion. CO_2 is a linear molecule with a strong C=O double bond and a significant quadrupole moment, which allows it to interact with charged or polar surfaces through electrostatic forces as well as through chemical bonding. On metal oxide surfaces, CO_2 adsorption typically occurs through two principal mechanisms: physisorption, driven by weak electrostatic or van der Waals interactions, and chemisorption, which involves the formation of carbonate or bicarbonate species. In Figure 3, first-principles investigations for ABO_3 (001) have shown that CO_2 binds strongly to AO-terminated surfaces with adsorption energies of approximately −1.73 to −1.33 eV and −1.89 to −1.48 eV, although −1.38 to −1.31 eV and −1.53 to −1.47 eV for BO_2-terminated surface of $BaTiO_3$ and $SrTiO_3$, respectively.[45] Those adsorbed CO_2 molecules form stable CO_3^{2-} species. Beyond this chemical bonding, the high dielectric properties inherent to $BaTiO_3$ create a unique environment for gas interaction. Ferroelectric perovskites provide a unique mechanism for CO_2 adsorption due to the presence of spontaneous polarization at the surface. In materials such as bulk

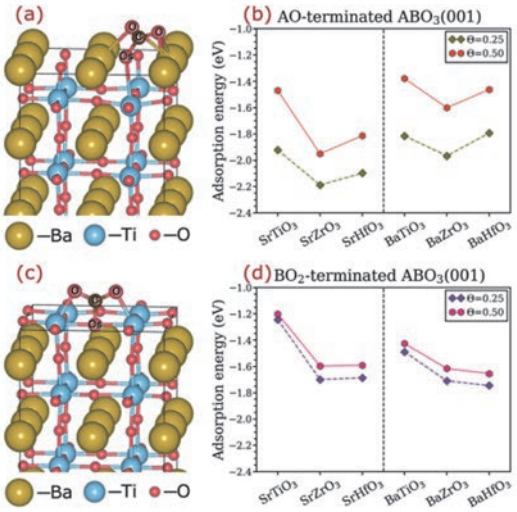

Figure 3. Most stable CO_2 adsorption conformations on (a) BaO- and (c) TiO_2-terminated $BaTiO_3$ (001) surfaces corresponding to $\theta = 0.25$. Computed CO_2 adsorption energies for the (b) AO- and (d) BO_2-terminated ABO_3(001) surfaces. Reprinted from ref. [45]. Copyright © 2018 Royal Society of Chemistry.

$BaTiO_3$, the surface electric field associated with ferroelectric polarization can interact with approaching CO_2 molecules which have quadrupole moments, facilitating adsorption. Experimental studies on $BaTiO_3$(001) surfaces have shown that CO_2 can adsorb in molecular form and subsequently form CO_3-like species through bonding between the carbon atom of CO_2 and surface oxygen anions. The initially linear CO_2 molecule becomes distorted during this process, forming a bent CO_3-like configuration stabilized by the surface polarization. In addition, the adsorbed species can contribute to the compensation of polarization charge at the ferroelectric surface, indicating a coupling between adsorption and the ferroelectric state of the material. These results suggest that ferroelectric polarization can significantly enhance CO_2 adsorption on perovskite oxide surfaces.[31]

The CO_2 adsorption mechanism on perovskites typically transitions from physical to chemical interaction with increasing temperature. For $LaCoO_3$, physisorption in a 'supermobile' state dominates at 195–373 K (isosteric heat ≈ 18.8 kJ/mol), whereas chemisorption prevails at 373–673 K, with adsorption heats reaching 75.3 kJ mol^{-1}. In this higher temperature regime, infrared spectroscopy identifies the formation of bidentate and monodentate carbonates, along with bicarbonates from surface hydroxyl reactions, underscoring the strong temperature dependence of the adsorbed species' stability.[46] The surface chemistry of $LaMnO_{3+y}$ further illustrates the energetic heterogeneity of perovskite surfaces. Investigations using DFT and adsorption isotherms (298–473 K) reveal that CO_2 interaction occurs on multiple active sites, reflecting both basic and acidic surface characters. The strongest adsorption is associated with surface oxygen vacancies (F-centers) and La-cation sites, where CO_2 molecules bind strongly to lattice oxygen to form stable chemisorbed carbonates. Conversely, weaker interactions occur at various cationic sites (La and Mn), where CO_2 adsorbs in perpendicular or bridged configurations. This site-dependent behavior, often following a Freundlich isotherm, highlights the critical role of surface defects and cation-specific coordination in governing the reversibility of CO_2 capture.[47] First-principles calculations on $BaZrO_3$ (001) surfaces demonstrate that CO_2 chemisorption induces a significant structural evolution. Specifically, on the BaO-terminated surface, the formation of carbonate species is accompanied by the migration of Ba cations

toward the vacuum, effectively pulling the A-site metals out of the ideal surface plane. This 'protruding' carbonate structure is stabilized by substantial charge transfer and surface relaxation, allowing a stable carbonate overlayer to persist even under 400 ppm CO_2 up to approximately 700 K. These results reinforce the critical role of A-site barium migration in facilitating the transition from simple surface adsorption to a stable, elevated carbonate phase.[48] The kinetics of CO_2 sorption on perovskite oxides is significantly influenced by the material's microstructure and thermal history, as demonstrated in studies on $La_{0.1}Sr_{0.9}Co_{0.5}Fe_{0.5}O_{3-\delta}$ (LSCF) at high temperatures (700–900 ℃). Experimental results indicate that LSCF samples sintered at lower temperatures (900 ℃) possess a porous structure that facilitates fast sorption kinetics, which can be accurately described by a homogeneous carbonation reaction model. In contrast, samples sintered at higher temperatures (1200 ℃) develop a dense structure, where CO_2 sorption is governed by slower diffusion-controlled processes. These observations emphasize that for high-temperature applications such as membrane separations, controlling the porosity and sintering conditions is as vital as the chemical composition to ensure rapid gas diffusion and efficient carbonate formation.[49] The complex sorption behavior of perovskite oxides is further demonstrated in $Sr_{0.5}Ca_{0.5}Co_{0.5}Fe_{0.5}O_3$, where the mechanism shifts significantly at a threshold of approximately 750 ℃. Below this temperature, CO_2 capture follows classical gas–solid reaction theory, with sorption rates being strongly dependent on temperature and CO_2 pressure, while the total capacity remains relatively constant. However, above 750 ℃, the equilibrium capacity begins to decrease with increasing temperature, as the reaction products transition into solid solutions of $SrCO_3$/SrO and $CaCO_3$/CaO. This temperature-induced shift from a stable carbonate phase to a pressure-dependent equilibrium highlights the thermodynamic limits of perovskite sorbents in high-temperature applications.[50]

Beyond traditional ABO_3 perovskites, derivative materials such as alkali-metal-based titanates have emerged as promising candidates for high-temperature CO_2 capture, offering a means to overcome the kinetic and thermodynamic limitations inherent in simple oxide structures. A significant development in this field is the synthesis of $KNaTiO_3$, which serves as a representative example of how structural modifications can enhance sorption performance. Unlike many alkaline-earth-based perovskites that exhibit slower kinetics or decreased efficiency at low CO_2 partial pressures, $KNaTiO_3$ demonstrates a remarkably fast uptake rate and a high reversible sorption capacity. The synergistic effect of K and Na not only enhances the surface basicity but also facilitates rapid gas-solid interaction, and titanate acts as structural framework stabilizer, leading to excellent cycling stability. This shift toward alkali-doped perovskite-related structures highlights a strategic pathway for engineering sorbents that combine the thermal robustness of ceramics with the high reactivity required for efficient carbon capture from diverse industrial flue gases.[51]

While many studies on perovskites as CO_2 sorbents focus on high-temperature bulk absorption, the performance of these materials at low to intermediate temperatures has traditionally been limited by their extremely low specific surface area. However, recent advances in nanostructuring have revealed that $BaTiO_3$ can be synthesized in nanoscale using carbon template method. By utilizing the slit-shaped micropores of activated carbon fibers (ACFs) as a template for the synthesis of $BaTiO_3$, crystal growth is effectively confined, resulting in the formation of ultra-fine $BaTiO_3$ nanoparticles with diameters of approximately 1–4 nm. Since the crystal growth is directed along the two-dimensional slit pores, the obtained $BaTiO_3$ exhibits a more pronounced structural anisotropy compared to particles synthesized via conventional sol–gel methods.[38, 52] Furthermore, when using the one-dimensional (1D) internal channels of carbon nanohorns (CNHs) as a template, the dimensionality of the resulting crystals can be precisely controlled by the synthesis procedure. A 1-step precursor introduction leads to the formation of zero-dimensional (0D) nanoparticles. In contrast, a 2-step method, where TiO_2 is first synthesized as a precursor followed by the introduction of the Ba source, yields one-dimensional (1D) nanostructures. This is attributed to the crystals growing preferentially along the 1D pores of the CNHs. The 1D particles obtained via this 2-step process exhibit a high aspect ratio, with dimensions typically ranging from 2–3 nm in width to 20–60 nm in length, shown in Figure 4.[53]

Owing to this technique, nanoscale $BaTiO_3$ can be transformed into a highly efficient CO_2 adsorbent through precise morphology control, bridging the gap between physisorption and chemical reaction. By fabricating nanoscale $BaTiO_3$ ceramics via carbon-template-solvothermal reactions, the specific surface

area can be dramatically increased (e.g., from 2 to ~270 m^2 g^{-1}), revealing these high-affinity sites. In fact, a defining feature of these nanoscale $BaTiO_3$ ceramics is their exceptional CO_2 adsorption behavior across a wide temperature range. Conventional solid-state synthesis, sol-gel synthesis, and ACF-templated sol-gel synthesis could produce different $BaTiO_3$ samples named as macro-, meso-, and nano-$BaTiO_3$ according to their sizes, respectively. Unlike conventional porous materials whose adsorption capacity drops sharply with temperature, nano-$BaTiO_3$ maintains significant adsorption density even at elevated temperatures such as 363 K (Figure 5).[38] This thermal stability is a result of the unusually strong affinity between the CO_2 molecules and the perovskite surface, likely enhanced by the interaction between the CO_2 quadrupole moment and the localized surface fields. Furthermore, the adsorption-desorption isotherms exhibit a remarkably large adsorption hysteresis. This non-reversible behavior suggests that the interaction is not a simple physical process but involves a significant energy barrier or a localized phase transition within the confined geometry of the nanopores. The nature of this interaction has been further elucidated through in-situ X-ray diffraction (XRD) analysis. Under CO_2 atmospheres, new diffraction peaks corresponding to solid-phase CO_2 have been observed (Figure 6).[38] This provides compelling evidence that CO_2 molecules are not merely forming a surface monolayer but undergoing a condensation-like process into a solid-like state within the nanopores. The stabilization of such a dense phase at these temperatures is attributed to the intense potential field provided by the $BaTiO_3$ surface and pore. It is considered that nanoscale $BaTiO_3$ forms particle morphology, and the spaces between particles act as pores. It should be noted, however, that while nanostructuring enhances these surface-driven adsorption properties, the reduction in crystal size toward the nanoscale typically leads to a transition from a tetragonal to a cubic-like symmetry, resulting in the suppression of the long-range spontaneous polarization characteristic of bulk $BaTiO_3$.[54, 55] Experimental evidence using XPS and TDS on nanostructured titanate surfaces further confirms that CO_2 chemisorbs at room temperature, with thermal desorption occurring between 423 and 723 K.[33] These results, combined with the discovery of solid-like CO_2 formation in nanoporous regions, indicate that nanoscale $BaTiO_3$ functions through a hybrid mechanism: it utilizes high surface area for rapid kinetics at low-to-medium temperatures, while maintaining the strong chemical affinity.

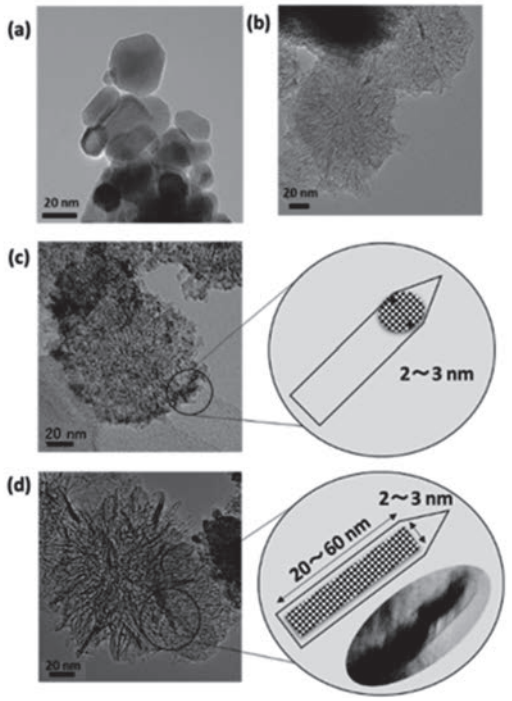

Figure 4. TEM images of 3D-$BaTiO_3$ (a), CNH (b), 0D-$BaTiO_3$ (c), and 1D-$BaTiO_3$ (d). Schematic images of $BaTiO_3$ synthesized in a CNH particle were depicted in the right of (c) and (d). Mosaic represents $BaTiO_3$ nanocrystals. Reprinted from ref. [53]. Copyright © 2017 The Carbon Society of Japan.

In summary, CO_2 interaction with perovskite surfaces is governed by a complex interplay of electrostatic forces, defect chemistry, and surface cation coordination. The development of nanoscale $BaTiO_3$ demonstrates that moving away from bulk properties toward surface-dominated regimes allows for high-capacity, thermally stable CO_2 capture. By leveraging the unique surface potential and nanoporous structures, these materials achieve a state of localized CO_2 solidification, offering a promising strategy for efficient carbon management at moderate operating conditions.

3. Thermochemical CO_2 Conversion over Perovskite-type Oxides with Reducing Gases

The thermochemical conversion of CO_2 using perovskite oxides as catalysts or oxygen carriers is a key strategy for producing synthetic fuels and chemicals. In these systems, the presence of a reducing gas—most commonly H_2—drives the catalytic cycle by facilitating the continuous regeneration of active sites within the perovskite lattice.

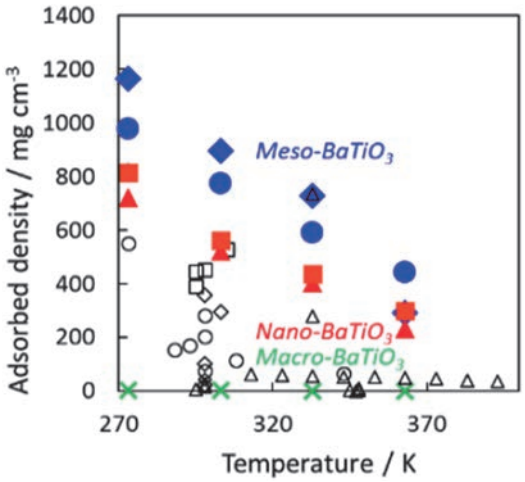

Figure 5. CO_2 adsorption densities in nanopores of $BaTiO_3$ crystals and other porous materials at 100 kPa. Macro- (green), meso- (blue), and nano-$BaTiO_3$ (red) are depicted. Carbon materials (○), metal-organic frameworks (◇), zeolites (□), and porous silica (△) are also depicted. Reprinted from ref. [38]. Copyright © 2017 Trade Science Inc.

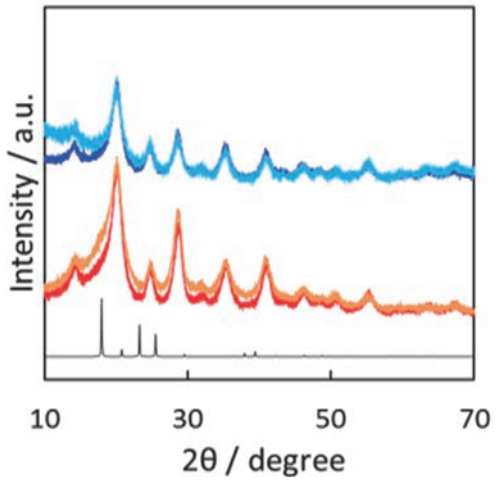

Figure 6. XRD patterns of meso-$BaTiO_3$ crystal (dark blue), meso-$BaTiO_3$ crystal adsorbing CO_2 (light blue), nano-$BaTiO_3$ crystal (red), nano-$BaTiO_3$ crystal adsorbing CO_2 (orange), and CO_2 solid (black) at 1 GPa. Reprinted from ref. [38]. Copyright © 2017 Trade Science Inc.

3.1. Fundamental Mechanisms: The Mars-van-Krevelen-like Chemical Looping Pathway in RWGS

The primary pathway for CO_2 conversion in the presence of H_2 is the Reverse Water-Gas Shift (RWGS) reaction ($CO_2 + H_2 \Rightarrow CO + H_2O$). Over perovskite catalysts, this reaction typically follows the Mars-van Krevelen (MvK) -like mechanism, which is centered on the dynamic behavior of lattice oxygen. The chemical looping begins with the reduction of the perovskite surface by heating with H_2, where H_2 reacts with lattice oxygen ($O_{lattice}$) to form steam (H_2O), leaving behind an oxygen vacancy (V_O). In the subsequent step, a CO_2 molecule adsorbs onto this vacancy site. The high oxygen affinity of the reduced perovskite facilitates the dissociation of the C=O bond; the vacancy splits an oxygen atom from CO_2 to restorable the lattice, while CO is released into the gas phase. The efficiency of this mechanism depends heavily on the oxygen vacancy formation energy and the oxygen mobility within the ABO_3 structure.[56-58]

3.2. Specific Examples and Catalytic Systems for RWGS

Various perovskite compositions have been tailored to optimize the RWGS process which generally requires high temperature above 600 ℃ for reduction step; production of oxygen vacancies in Figure 7.[59] As potential materials, ferrite-based perovskites such as $La_{1-x}Sr_xFeO_{3-\delta}$ (LSF) are widely studied for their high thermal stability and significant oxygen non-stoichiometry. Cobalt-containing oxides like $LaCoO_3$ have also shown high activity, where the calcination temperature and the resulting surface area significantly influence the reduction-oxidation kinetics. Recent studies have demonstrated that substituting the B-site with transition metals (e.g., Ni, Cu, or Fe) can lower the operating temperature and increase CO selectivity.[58] These materials often act as “intelligent catalysts” where, under reducing conditions, a fraction of the B-site metal can migrate to the surface to form highly dispersed, metallic nanoparticles (exsolution), further accelerating the H_2 dissociation and CO_2 activation steps.[60, 61]

The reduction of $LaCoO_3$ and $LaCo_{0.5}Fe_{0.5}O_3$ follows a contracting volume model, with activation energies on the order of 70–90 kJ mol^{-1}, while the subsequent CO_2 oxidation step exhibits higher activation barriers (~149 kJ mol^{-1}). Notably, the CO_2 splitting reaction is strongly influenced by particle size, with smaller particles showing enhanced conversion rates due to their higher

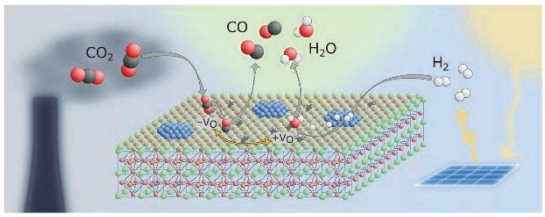

Figure 7. Schematic diagram of chemical looping RWGS reaction. Reprinted from ref [59]. Copyright © 2021 Elsevier.

surface-to-bulk ratio and the increased availability of reactive surface sites. Furthermore, XPS analysis indicates that the redox cycle is primarily governed by changes in the Co oxidation state, highlighting the role of transition metal cations in facilitating oxygen exchange during CO_2 conversion.[62] Recent work on Ca/Mn co-doped $LaNiO_3$ further demonstrates that compositional engineering can significantly enhance RWGS-CL performance, achieving an oxygen transfer capacity of 1.97 $mmolO_2\ g^{-1}$ and up to 57% CO_2-to-CO conversion at 900 ℃. Notably, syngas with an H_2/CO ratio of 2.0 suitable for Fischer–Tropsch synthesis was obtained at 600 ℃, while CO_2 sorption was also confirmed via carbonation–calcination cycles. These results highlight that A- and B-site doping not only improves redox kinetics but also enables integrated CO_2 capture and conversion functionalities in perovskite oxides.[63] Lindenthal et al. demonstrated that exsolution of Ni or Co nanoparticles from perovskite host lattices (e.g., $Nd_{0.6}Ca_{0.4}Fe_{0.9}Ni_{0.1}O_{3-\delta}$) significantly enhances RWGS activity. The exsolved catalyst achieved high CO_2 conversion exceeding 20% at 600 ℃, with nearly 100% CO selectivity. This superior performance and stability are attributed to the strong anchoring of nanoparticles in the perovskite support, which prevents sintering and promotes efficient CO_2 activation via a Mars-van Krevelen-like mechanism (Figure 7).[59]

The dry reforming of methane (DRM) is recognized as a significant alternative route for CO production. Operating typically at 700–800 ℃, this process ($CH_4 + CO_2 \rightarrow 2CO + H_2$) is often accompanied by the RWGS reaction, which can influence the final H_2/CO ratio. Especially, Ni-perovskites, such as $LaNiO_3$, serve as excellent precursors that exsolve highly dispersed Ni nanoparticles in situ, providing abundant active sites while suppressing carbon coking. Furthermore, the incorporation of alkaline-earth metals like Sr or Ca enhances the surface alkalinity, which promotes CO_2 adsorption and facilitates the removal of carbon species from the Ni surface, ensuring long-term stability and high syngas yields.[64] $La_{1-x}Sr_xNiO_3$ perovskites were tested as catalyst precursors for dry reforming of methane at 700 ℃. Among them, $LaNiO_3$ exhibited the highest activity, following the order: $LaNiO_3 > La_{0.6}Sr_{0.4}NiO_3 > La_{0.9}Sr_{0.1}NiO_3$. The high stability and lack of carbon formation are attributed to the formation of $La_2O_2CO_3$ and $SrCO_3$ phases during the reaction, which facilitate La_2O_3 regeneration and improve reforming performance.[65]

3.3. Technological Evolution: Solar-Driven Two-Step Thermochemical Chemical Looping

As an eco-friendly evolution of the catalytic RWGS process, researchers are integrating perovskites into solar-driven two-step thermal chemical looping. This approach utilizes concentrated solar energy to replace or augment chemical reduction, effectively converting solar heat into chemical energy (Solar-to-Fuel).[25, 66, 67] In this technological framework, the reduction step is driven by intense solar thermal energy (typically > 1,200 ℃), which thermally induces the formation of a high density of oxygen vacancies. The oxidation step then uses CO_2 to refill these vacancies, producing a high-purity stream of CO as well. By coupling this cycle with solar-generated H_2 from water splitting, a sustainable source of syngas (CO + H_2) is produced. Perovskites such as $La_{1-x}Sr_xMnO_{3-\delta}$ (LSM) are favored in this evolution because they can achieve significant reduction at lower temperatures than traditional ceria-based systems, enhancing the overall solar-to-thermal energy conversion efficiency.[68, 69] Another effective strategy involves the use of core-shell architectures to enhance both reactivity and structural integrity. Lee et al. developed a Fe_2O_3@$La_{0.7}Sr_{0.3}FeO_3$ (LSF) core-shell oxygen carrier for RWGS chemical looping. In this system, the LSF shell facilitates rapid oxygen ion transport while preventing the sintering of the Fe_2O_3 core during the reduction (H_2) and oxidation (CO_2 splitting) cycles at 600 ℃, leading to high CO selectivity and stable cyclability.[70] While solar-thermal strategies leverage concentrated solar energy to drive the endothermic RWGS reaction, recent advancements have expanded the scope of CO_2 conversion by utilizing other external fields.[71] These approaches include light, electric, photothermal, electromagnetic, and plasma fields, each offering distinct mechanisms for CO_2 activation and conversion. For instance, photocatalytic systems utilize photoinduced electron–hole pairs to drive CO_2 reduction under mild conditions, often employing H_2O as a reductant instead of H_2, thereby fundamentally differing from thermocatalytic RWGS pathways.[72] Electrocatalytic processes, on the other hand, enable precise control over reaction energetics through applied potential, facilitating CO production with high selectivity and compatibility with renewable electricity sources. Thalinger et al. demonstrated that the RWGS reaction on $La_{0.6}Sr_{0.4}FeO_{3-\delta}$ (LSF) can be electrochemically accelerated. By applying a cathodic potential at 600 ℃, they shifted the surface

oxygen chemical potential and increased oxygen vacancy concentration, significantly enhancing CO_2 activation kinetics compared to conventional thermal conditions.[73] In addition, photothermal and photoelectric coupling strategies synergistically combine thermal and non-thermal effects to enhance reaction rates and lower energy input requirements.[74] More recently, plasma-assisted and electromagnetic field-driven systems have attracted attention due to their ability to generate highly reactive species (e.g., radicals, excited molecules), enabling CO_2 conversion under relatively low bulk temperatures and non-equilibrium conditions.[75, 76] A hybrid dielectric barrier discharge (DBD) plasma-catalysis system achieved RWGS at < 150 ℃, with $La_{0.9}Sr_{0.1}Ni_{0.5}Fe_{0.5}O_{3+\delta}$ showing the highest CO selectivity. Its performance stems from Ni-Fe alloy formation enhancing CO_2 adsorption and oxygen vacancies in the perovskite structure promoting selective reduction.[77] Collectively, these external-field-driven methodologies provide promising pathways to achieve efficient CO_2-to-CO conversion under milder and more sustainable conditions compared to traditional thermal catalysis.

3.4. Diversification of Products: Beyond RWGS

While CO is the primary product of RWGS, perovskite-derived catalysts are increasingly used for deep hydrogenation and complex hydrocarbon synthesis:

Methanation: Perovskite-derived catalysts enable a reductive pathway of CO_2 into CH_4 according to the equation as follows: $CO_2 + 4H_2 \rightarrow CH_4 + 2H_2O$.[78] Barreau et al. demonstrated that $LaNiO_3$ perovskite achieves superior CO_2 methanation activity with nearly 100% CH_4 selectivity, reaching thermodynamic equilibrium at 400 ℃. The catalyst exhibits a 100 ℃ lower T_{50} compared to impregnated Ni/La_2O_3 and maintains stability for 65 hours at 300 ℃, with Ni nanoparticles (~6 nm) anchored via "socketing." This enhanced performance is driven by the in situ formation of $La_2O_2CO_3$ as a key intermediate for CO_2 activation.[79] Also, Ru-substituted $LaNi_{0.9}Ru_{0.1}O_3$ perovskites, particularly when supported on Al_2O_3, exhibit exceptional CO_2 methanation performance. The catalyst achieved 100% CO_2 conversion and 100% CH_4 selectivity at 350 ℃, with a significantly high reaction rate of 1112.5 $\mu molCO_2\ gcat^{-1}\ s^{-1}$. This enhanced activity is attributed to the synergistic effect between exsolved Ni and Ru nanoparticles, which promotes H_2 dissociation and CO_2 activation, maintaining stable performance over 50 hours without significant deactivation.[80]

Methanol Synthesis: Perovskites are increasingly utilized as precursors for methanol synthesis catalysts. A reaction that eliminates the intermediate step via gas synthesis is direct methanol synthesis using CO_2 and H_2 according to equation as follows: $CO_2(g) + 3H_2(g) \rightleftharpoons CH_3OH(g) + H_2O(g)$ ($\Delta H = -50\ kJ \cdot mol^{-1}$).[81] The equation clearly shows that high pressures favour the reaction and are therefore needed for good yields. For instance, Poerjoto et al. investigated $La_{1-x}Sr_xCuO_3$ perovskite-derived catalysts for CO_2 hydrogenation to methanol. Among the series, $La_{0.9}Sr_{0.1}CuO_3$ exhibited the highest performance, achieving a methanol selectivity of 84% and a yield of 1.4% at 250 ℃ and 3.0 MPa. The study highlights that the substitution of Sr^{2+} creates more oxygen vacancies and enhances surface basicity, which optimizes CO_2 adsorption strength. This superior activity is attributed to the balanced interaction between the Cu active sites and the lattice oxygen mobility, facilitating the selective hydrogenation of CO_2 to methanol while suppressing the RWGS side reaction.[82] Schrenk et al. investigated Cu-doped perovskites (e.g., $Nd_{0.6}Ca_{0.4}Fe_{0.97}Cu_{0.03}O_{3-\delta}$) as catalysts for CO_2 hydrogenation to methanol. The study demonstrates that exsolution of Cu nanoparticles at 600 ℃ significantly enhances catalytic activity compared to traditionally prepared Cu catalysts. Under reaction conditions of 230 ℃ and 15 bar, the exsolved catalysts achieved high methanol selectivity and stability. The superior performance is attributed to the strong interaction between the metallic Cu nanoparticles and the perovskite host, which facilitates efficient CO_2 activation while maintaining a high dispersion of active sites.[81]

Higher Hydrocarbons (C^{2+}): Beyond C1 products, the selective hydrogenation of CO_2 into value-added C^{2+} hydrocarbons represents a more complex but rewarding frontier in CO_2 utilization. Wang et al. investigated this transformation using a hybrid DBD plasma-catalysis system with $La_{1-x}Ca_xNiO_3$ perovskites. Among the tested compositions, the $La_{0.7}Ca_{0.3}NiO_3$ catalyst exhibited the best performance, achieving a CO_2 conversion of 32.5% and a C2-C4 hydrocarbon selectivity of 23.3%. The study reveals that Ca-doping creates crystal defects and increases the amount of adsorbed oxygen and weak basic sites, which cooperatively facilitate the Fischer-Tropsch-like chain growth of carbon species under plasma-enhanced conditions.[83] In summary, thermochemical CO_2 conversion over perovskite-type

oxides is driven by the dynamic exchange of lattice oxygen and the high mobility of oxygen vacancies. Recent advancements in metal exsolution techniques have further enhanced the durability and activity of these catalysts by anchoring metallic nanoparticles within the perovskite matrix, preventing sintering even under harsh thermal conditions. By optimizing B-site cation substitution and oxygen non-stoichiometry, perovskite oxides serve as highly tunable platforms for CO_2 utilization via RWGS and methane reforming, bridging the gap between traditional catalysis and sustainable energy systems like solar-thermal cycles.

4. Thermochemical CO_2 Conversion over Perovskite-type Oxides without Reducing Gases

While Chapter 3 detailed the effectiveness of perovskites in the RWGS, methanation, and other reactions, these processes remain fundamentally dependent on the availability of reducing gas such as H_2. Current industrial hydrogen production—predominantly via steam methane reforming—is carbon-intensive, emitting between 0.5-13 kg-CO_2 / kg-H_2 produced.[84] Consequently, there is an urgent technological imperative to develop CO_2 conversion pathways without the requirement of external reducing gases.

4.1. Thermal CO_2 splitting using 2-Step Chemical Looping

To further advance carbon-neutral cycles, direct CO_2 conversion methods that do not require external reducing gases—specifically thermochemical CO_2 splitting—have emerged as a critical frontier. CO_2 is a thermodynamically stable molecule, requiring significant energy input to break the C=O bond as mentioned above. Perovskite oxides offer a versatile platform for this challenge due to their exceptional lattice oxygen mobility and structural stability, allowing for the fine-tuning of oxygen vacancy formation and redox properties through cation substitution.

Direct thermolysis represents the most straightforward approach to CO_2 dissociation into CO and O_2. Jiang et al. demonstrated that this reaction can occur at temperatures as low as 1200 ℃ within a corundum tube. Crucially, they found that the presence of metal oxides can enhance the reaction rate by several times, a phenomenon attributed to the catalytic role of oxygen vacancies within the oxide lattice in Figure 8. This suggests that perovskite materials, known for their high vacancy concentrations, could significantly lower the kinetic barriers associated with one-step thermolysis.[10]

To bypass the high temperatures and gas separation issues associated with direct thermolysis, two-step solar thermochemical cycles have been developed as well as RWGS route. This process involves the thermal reduction of the perovskite at high temperatures to create oxygen vacancies, followed by a lower-temperature re-oxidation step where CO_2 is split to replenish the lattice oxygen and produce CO. Nair and Abanades performed an extensive screening of various perovskite and Ruddlesden-Popper (RP) structures to identify efficient redox materials. Their study highlighted that $La(B,B')O_3$ perovskites—specifically those containing combinations of Mn with Ni or Co—along with strontium-doped lanthanum manganites ($La_{0.5}Sr_{0.5}MnO_3$), exhibit superior performance. Notably, RP-structured materials such as $LaSrMnO_4$ and $LaSr_2Mn_2O_7$ demonstrated remarkable thermochemical stability and consistently higher CO yields compared to standard perovskites, even without morphological optimization.[43] The redox capacity can be further enhanced through strategic doping at the B-site. For instance, Zr-doped $LaCoO_3$ perovskites have shown promising results for solar-driven CO production. Research indicates that $LaCo_{0.7}Zr_{0.3}O_3$ serves as an optimum composition, yielding an average of 1066.6 μ mol g^{-1} of CO. This material exhibits a relatively low activation energy for the reduction reaction (107.1 kJ mol^{-1}), which is significantly lower than that of conventional CeO_2, enabling more efficient operation at lower thermal budgets.[85] Integrating perovskites into more complex redox schemes can further lower the required operating temperatures. Zhang et al. reported a cyclic redox scheme using iron-containing perovskite nanocomposites where methane was introduced as an

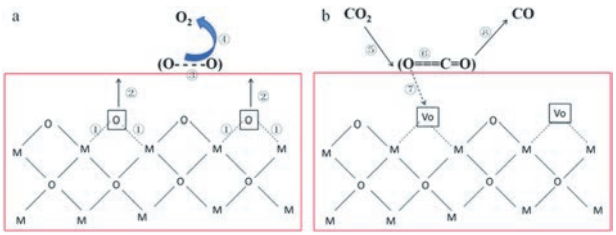

Figure 8. A possible catalytic mechanism for the direct CO_2 splitting reaction in the presence of redox metal oxides. It is composed of two key processes: (a) the formation of oxygen vacancies in the metal oxides at high temperatures and (b) the dissociative adsorption of CO_2 on the defective surfaces. Reprinted from ref. [10]. Copyright © 2017 Royal Society of Chemistry.

"oxygen sink" during the reduction step. By coupling methane partial oxidation with CO_2 splitting, they achieved near 100% CO_2 conversion to CO at temperatures between 900 and 980 ℃. Remarkably, the CO production rate in this system was approximately seven times higher than that of state-of-the-art solar-thermal splitting processes that typically require temperatures exceeding 1200 ℃.[86]

4.2. CO_2 decomposition via nanoscale perovskite oxides

While the chemical looping schemes discussed previously are effective, they inherently require a high-temperature reduction phase (often exceeding 1000–1200 ℃) to thermally regenerate oxygen vacancies. These high-temperature requirements lead to material sintering and reduced net energy efficiency. To bridge this gap, recent research has focused on continuous catalytic CO_2 decomposition using nanostructured perovskite oxides. By reducing $BaTiO_3$ dimensions to the sub-20 nm scale, it becomes possible to achieve direct CO_2 thermolysis at temperatures far below the traditional bulk threshold without the need for external reducing gases like H_2.

4.2.1. Synthesis of High-Value Carbons via Nanosizing of ABO_3

The feasibility of reducing CO_2 to solid carbon species, specifically graphitic and diamond-like carbons using perovskite-type titanium nanocatalysts ($BaTiO_3$, $SrTiO_3$, $CaTiO_3$ and $PbTiO_3$) was established at 700 K under ambient pressure. TEM images reveal the carbon layer on the perovskite oxide surface after CO_2 reaction in Figure 9. The higher CO_2 reactivity can be attributed to the factors as below.

● Size-Dependent Reactivity:

A critical discovery was the exponential increase in CO_2 reduction activity as the catalyst crystal size decreased below 20 nm. Figure 10 indicates that nanocatalysts with a size of approximately 10 nm (corresponding to 100–230 $m^2\ g^{-1}$) exhibited exceptionally high reaction yields (400–1100 μmol g^{-1}), which are comparable to the performance of high-temperature bulk systems.

● The Quasi-High-Pressure Mechanism:

In addition to particle size contribution, this low-temperature activity is attributed to a quasi-high-pressure reaction state.[87, 88] Within the nanopores formed by the aggregation of 10 nm particles, CO_2 molecules undergo frequent collisions with the pore walls and each other. In fact, Figure 11 represents that micropore volume against reacted CO_2 amount correlated well with $R^2 = 0.97$, although specific surface area and total pore volume against reacted CO_2 amount have R^2 value of 0.93 and 0.44, respectively. This molecular confinement creates a localized environment where the effective pressure is significantly higher than the ambient atmosphere, thermodynamically facilitating

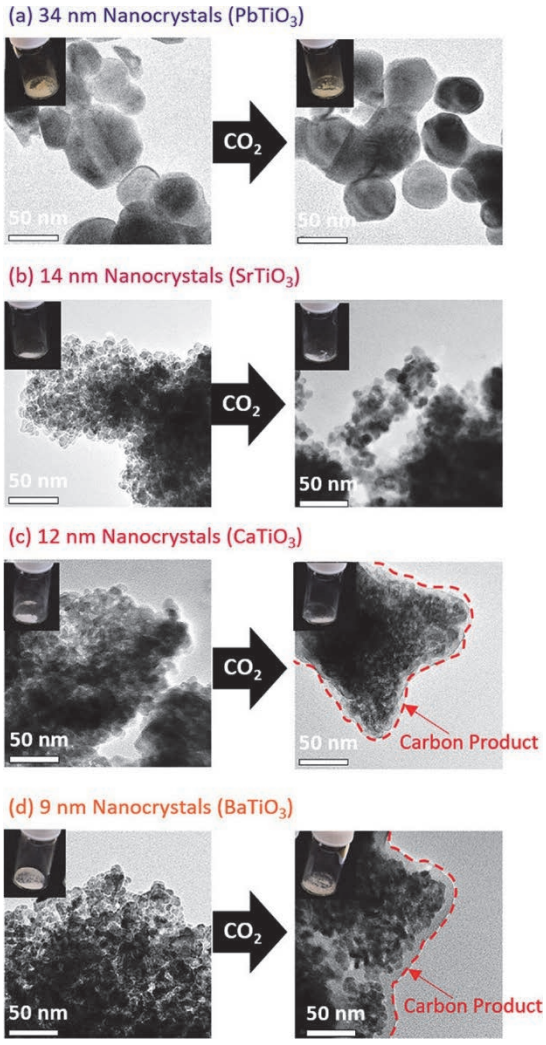

Figure 9. Deposition of solid carbon products on nanocatalysts as a result of CO_2 thermal reduction. Transmission electron microscopy images were collected before (left) and after (right) exposure to CO_2 gas at 700 K for 24 h of nanocatalysts $PbTiO_3$-34 nm (a), $SrTiO_3$-14 nm (b), $CaTiO_3$-12 nm (c), and $BaTiO_3$-9 nm (d). Black particles were nanocatalysts, and gray transparent films on nanocatalysts indicated solid carbon products. Red dashed curves in (c) and (d) represent the interfaces of solid carbon products. The insets in each TEM image show the photo images of nanocatalysts. Reprinted from ref [33]. Copyright © 2021 ACS Publications.

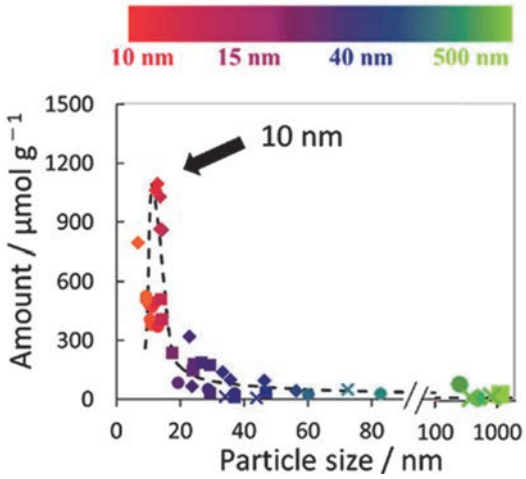

Figure 10. Amount of CO_2 reacted by thermal reduction as a function of particle size for $BaTiO_3$ (●), $CaTiO_3$ (◆), $SrTiO_3$ (■), and $PbTiO_3$ (×) nanocatalysts. Colors indicate the approximate particle size. Adapted from ref. [33]. Copyright © 2021 ACS Publications.

the endothermic reduction of CO_2 to solid carbon such as graphitic carbon and nanodiamond with oxygen at 700 K (Figure 12).[33]

4.2.2. Temperature-Dependent Reaction Pathways

To understand the kinetics and the transition from adsorption to decomposition, the interaction between CO_2 and $BaTiO_3$ nanocatalysts was evaluated across a wide temperature range of 300 to 1000 K. Comprehensive analyses using thermogravimetry (TG), X-ray photoelectron spectroscopy (XPS), transmission electron microscope (TEM), and temperature-programmed reaction mass spectrometry (TPR-MS) revealed four distinct temperature-dependent reaction regimes (summarized in Figure 14):

300–550 K (Sorption Phase): CO_2 primarily undergoes adsorption onto the $BaTiO_3$ surface (CO_2 → $CO_{2,ads}$ on $BaTiO_3$). While physical adsorption is dominant at 300 K, it gradually transitions toward chemisorption as the temperature rises.

550–800 K (Carbon Formation Phase): In this regime, dissociative chemisorption leads to the direct thermal reduction of CO_2 into solid carbon and oxygen (CO_2 → $C + O_2$). XPS and TEM (Figure 13) observations confirmed the deposition of graphitic and diamond-like carbon structures on the nanocatalyst surface.

800–850 K (CO Production Phase): As the temperature increases further, the reaction pathway shifts toward the production of carbon monoxide (CO_2 to $CO + 1/2\ O_2$).

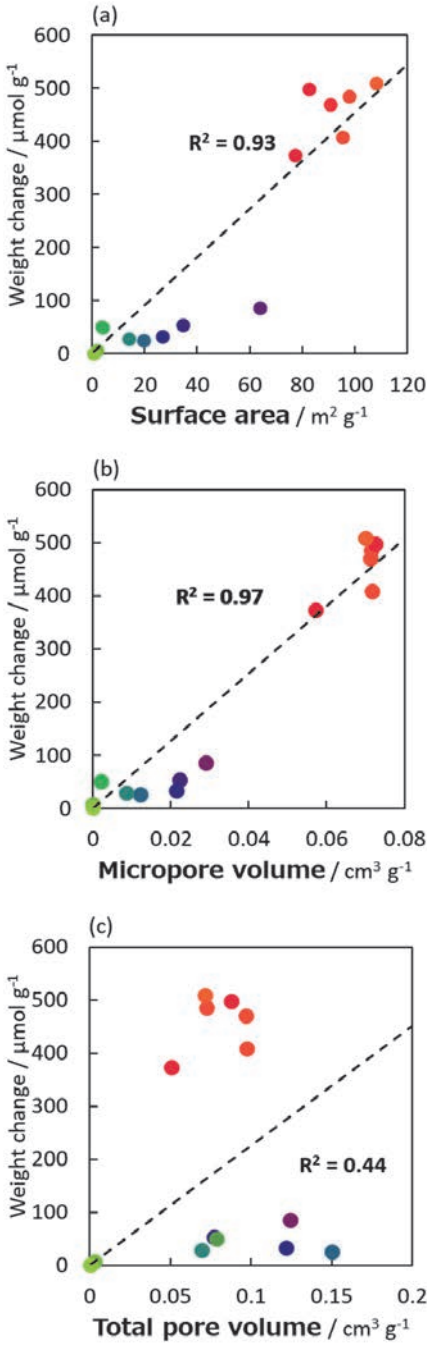

Figure 11. Correlation plots of (a) specific surface area, (b) micropore volume, and (c) total pore volume against weight change in CO_2 reaction at 700 K.

Above 850 K (Desorption and Gasification Phase): Beyond 850 K, CO_2 desorption occurs. Simultaneously, the deposited solid carbon reacts with gas-phase CO_2 via the reverse Boudouard reaction (CO disproportionation: $CO_2 + C$ → $2CO$), leading to significant CO evolution.

These findings demonstrate that the $BaTiO_3$ nanostructure acts as an active catalytic site that facilitates oxygen exchange and C=O bond cleavage, with the product selectivity (C vs. CO) being highly tunable via temperature control.[44]

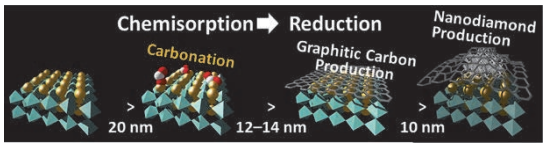

Figure 12. CO_2 chemisorption and reduction on nanocatalysts of different particle sizes. Reprinted from ref [33]. Copyright © 2021 ACS Publications.

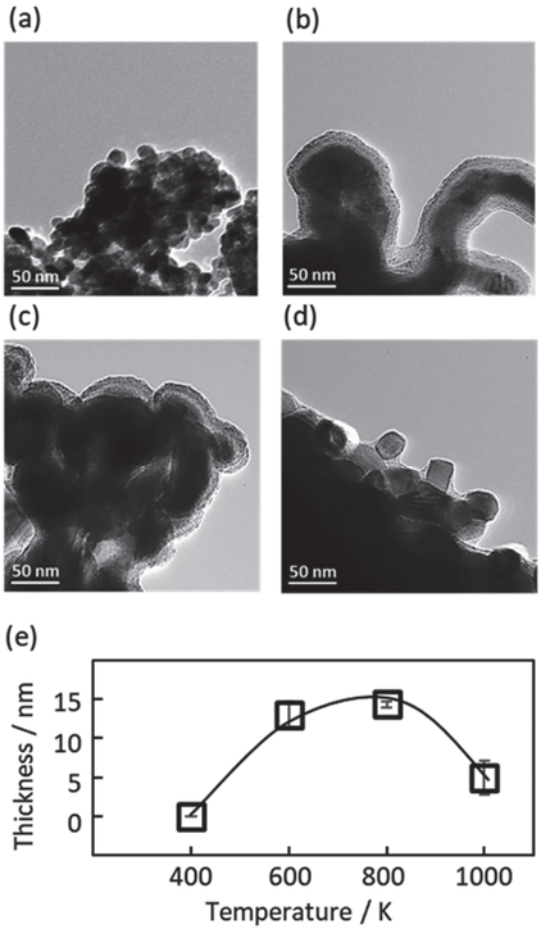

Figure 13. Carbon layer thickness as a function of temperature. TEM image of the 10-nm nanocatalysts exposed to CO_2 gas at (a) 400 K, (b) 600 K, (c) 800 K, and (d) 1000 K for 24 h. (e) Carbon layer thickness evaluated from the TEM images. Reprinted from ref. [44]. Copyright © 2022 Royal Society of Chemistry.

4.2.3. Influence of Pressure on CO_2 Decomposition

The pressure-dependent behavior of CO_2 thermolysis over $BaTiO_3$ nanocatalysts was systematically investigated at 700 K to evaluate the impact of molecular density on catalytic activity. The study reveals that CO_2 conversion yields are highly sensitive to the reaction pressure, with the 10 nm-nanocatalysts exhibiting a significant increase in carbon production within the optimal pressure range of 0.1 to 0.5 MPa, shown in Figure 15 and 16. This enhanced reactivity is attributed to the increased molecular density of CO_2 within the confined interparticle spaces, which facilitates the formation of a quasi-high-pressure state. While the 10 nm particles showed high sensitivity to pressure changes compared to larger 30 nm and 50 nm particles, it was observed that excessive pressurization up to 1.0 MPa led to a decrease in the carbon yield. These findings indicate that maintaining an appropriate pressure window of 0.1–0.5 MPa is crucial for maximizing the efficiency of H_2-free CO_2 reduction into valuable solid carbon products.[89]

Collectively, these studies establish that nanoscale engineering of perovskites fundamentally alters the thermodynamics and kinetics of CO_2 reduction. By leveraging size-induced surface effects and molecular confinement within aggregated nanostructures, these materials enable carbon-negative utilization at mild temperatures (700 K) without H_2 consumption. This represents a significant leap forward in developing energy-efficient carbon capture and utilization (CCU) technologies.

5. Conclusion

This review has highlighted the multifaceted potential of perovskite-type oxides, particularly $BaTiO_3$, as pivotal materials for the next generation of CO_2 capture and conversion technologies. By shifting the focus from bulk properties—which are often limited by thermodynamic constraints—to surface-dominated regimes through nanostructuring, it is possible to achieve high-density CO_2 adsorption and low-temperature conversion. The synergy between lattice defect engineering, such as oxygen vacancy control, and the utilization of unique surface potentials enables efficient CO_2 activation via both reductive and non-reductive pathways. Specifically, the discovery of direct CO_2 decomposition into solid carbon using sub-20 nm particles opens new avenues for carbon sequestration without relying on hydrogen or methane. Looking forward, the integration of these nanoceramic materials with renewable energy fields, alongside a deeper understanding of the atomic-scale interactions at the gas-solid interface, will be essential. Ultimately, the versatility and structural robustness of perovskites position them as a cornerstone in the development of a sustainable, closed-loop carbon economy.

References

[1] E. S. Sanz-Pérez, C. R. Murdock, S. A. Didas and C. W. Jones, *Chem. Rev.*, 2016, 116, 11840-11876.

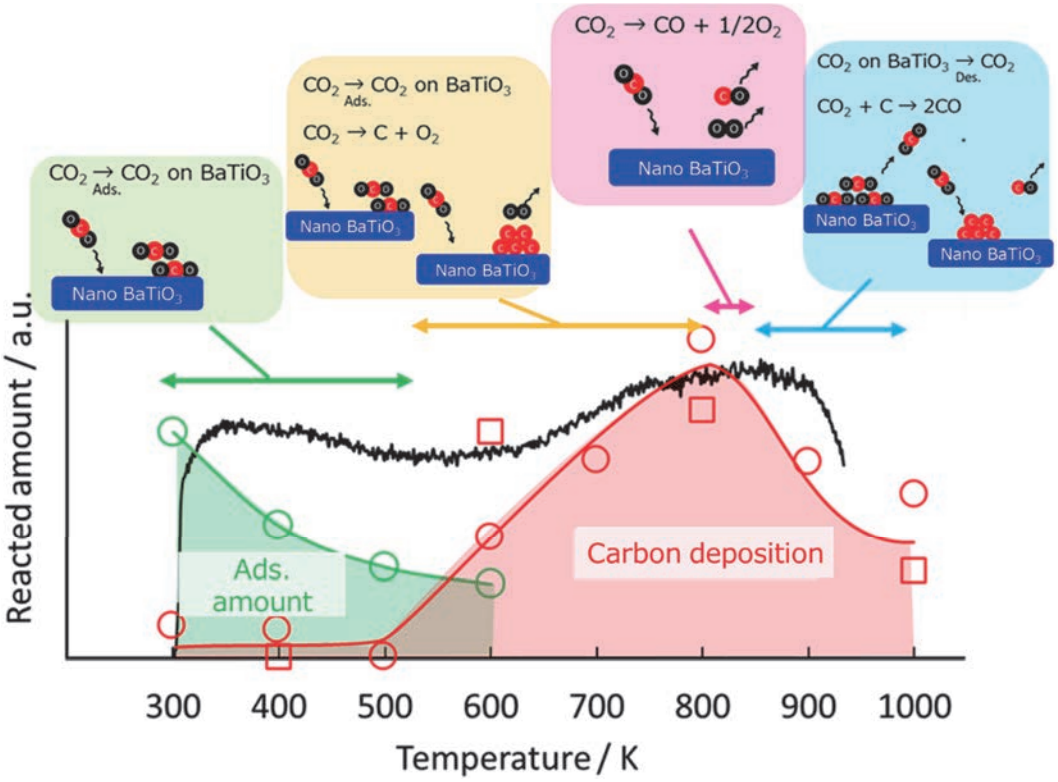

Figure 14. Temperature-dependent classification of CO_2 sorption/reaction on the $BaTiO_3$ nanocatalyst

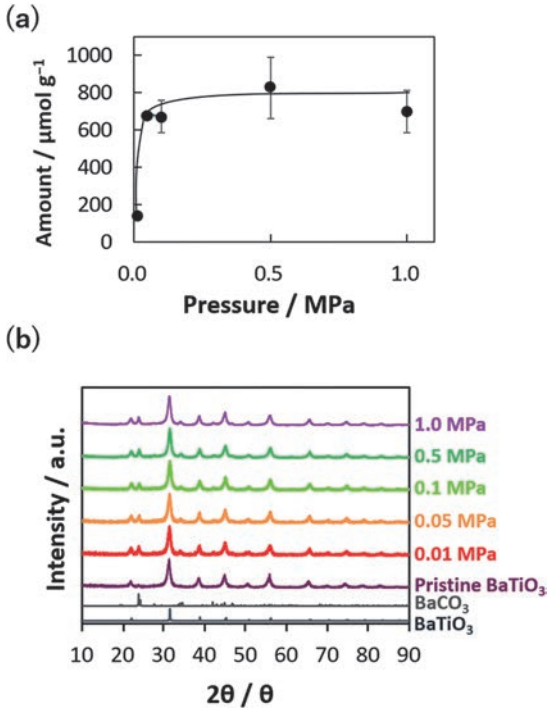

Figure 15. (a) Weight increase of nanocatalysts after CO_2 thermolysis at 0.01–0.5 MPa. (b) XRD patterns of barium titanate nanocatalysts after CO_2 thermolysis. XRD patterns of barium carbonate and crystalline barium titanate are also shown as references. Reprinted from ref. [89]. Copyright © 2024 Royal Society of Chemistry.

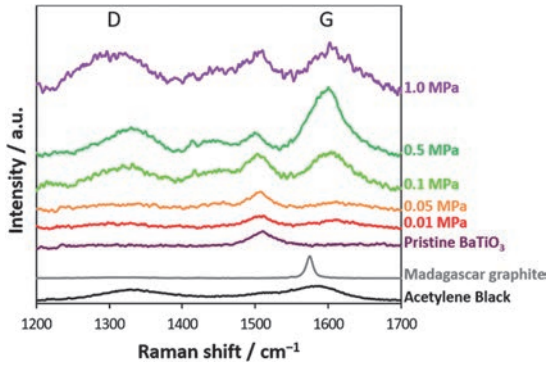

Figure 16. Raman scattering spectra of the nanocatalysts before and after CO_2 thermolysis. Raman scattering spectra of acetylene black and Madagascar graphite are shown for reference. Reprinted from ref. [89]. Copyright © 2024 Royal Society of Chemistry.

[2] Z. Deng, B. Zhu, S. J. Davis, P. Ciais, D. Guan, P. Gong and Z. Liu, *Nat. Rev. Earth Environ.*, 2025, 6, 231-233.

[3] J. D. Figueroa, T. Fout, S. Plasynski, H. McIlvried and R. D. Srivastava, *Int. J. Greenh. Gas Con.*, 2008, 2, 9-20.

[4] T. Ghanbari, F. Abnisa and W. M. A. Wan Daud, *Sci. Total Environ.*, 2020, 707, 135090.

[5] S. Foorginezhad, F. Weiland, Y. Chen, S. Hussain and X. Ji, *Renew. Sustain. Energy Rev.*, 2025, 215, 115589.

[6] I. Sognnaes and G. P. Peters, *Nat. Commun.*, 2025, 16, 8343.

[7] *Climate Change 2022 - Mitigation of Climate Change: Working Group III Contribution to the Sixth Assessment Report of the Intergovernmental Panel on Climate Change*, Cambridge

University Press, Cambridge, 2023.

[8] A. Kätelhön, R. Meys, S. Deutz, S. Suh and A. Bardow, *PNAS*, 2019, 116, 11187-11194.

[9] S. Gong, P. Wang and Y. Mo, *J. Phys. Chem. Lett.*, 2024, 15, 10842-10848.

[10] Q. Jiang, Z. Chen, J. Tong, M. Yang, Z. Jiang and C. Li, *Chem. Commun.*, 2017, 53, 1188-1191.

[11] W. Gao, Y. Zhu, Y. Wang, G. Yuan and J.-M. Liu, *J. Materiomics*, 2020, 6, 1-16.

[12] S. Chander and S. K. Tripathi, *Mater. Adv.*, 2022, 3, 7198-7211.

[13] W. L. Warren, K. Vanheusden, D. Dimos, G. E. Pike and B. A. Tuttle, *J. Am. Ceram. Soc.*, 1996, 79, 536-538.

[14] J. Yang, S. Hu, Y. Fang, S. Hoang, L. Li, W. Yang, Z. Liang, J. Wu, J. Hu, W. Xiao, C. Pan, Z. Luo, J. Ding, L. Zhang and Y. Guo, *ACS Catal.*, 2019, 9, 9751-9763.

[15] R. B. Wexler, G. S. Gautam, E. B. Stechel and E. A. Carter, *J. Am. Chem. Soc.*, 2021, 143, 13212-13227.

[16] K. Chu, W. Zong, G. Xue, H. Guo, J. Qin, H. Zhu, N. Zhang, Z. Tian, H. Dong, Y.-E. Miao, M. B. J. Roeffaers, J. Hofkens, F. Lai and T. Liu, *J. Am. Chem. Soc.*, 2023, 145, 21387-21396.

[17] V. Lantto, S. Saukko, N. N. Toan, L. F. Reyes and C. G. Granqvist, *J. Electroceram.*, 2004, 13, 721-726.

[18] M. Kim, S. Park, J. Ahn, J. W. Baek, D.-H. Kim, H. Shin, J. Ko, L. Song, C. Park, E. Shin and I.-D. Kim, *ACS Sens.*, 2024, 9, 6492-6501.

[19] C. Wei, Z. Guo, H. Wang, S. Zhang, D. Hao and J. Huang, *Mater. Horiz.*, 2025, 12, 317-342.

[20] R. J. H. Voorhoeve, D. W. Johnson, J. P. Remeika and P. K. Gallagher, *Science*, 1977, 195, 827-833.

[21] B. Wang, Y. Xuan, G. Zhu, Y. Liang, Y. Peng, Q. Chang, T. Luan, D. Wang and J. Li, *ACS Appl. Mater. Interfaces*, 2025, 17, 21168-21179.

[22] U. Bora, D. Lahon and L. Saikia, *Top. Catal.*, 2025, 68, 2255-2268.

[23] M. Hjiri and N. Mustapha, *Mol. Catal.*, 2026, 595, 115844.

[24] Y. Jiang, Y. Feng, A. Rastegarpanah, C. Liu, P. Chu, Z. Wang, L. Wei, Y. Liu, H. Dai and J. Deng, *Environ. Sci. Nano*, 2025, 12, 4491-4514.

[25] C. Liu, J. Park, H. A. De Santiago, B. Xu, W. Li, D. Zhang, L. Zhou, Y. Qi, J. Luo and X. Liu, *ACS Catal.*, 2024, 14, 14974-15013.

[26] K. J. Albrecht, G. S. Jackson and R. J. Braun, *Appl. Energy*, 2016, 165, 285-296.

[27] X. Liu, Y. Wang, W. Tian, F. Zhu, J. Wang, W. Wang, Y. Li, K. Zeng and J. Shi, *Small*, 2025, 21, 2409801.

[28] R. Wei, S. Li, A. Li and Y.-H. Lin, *Research*, 8, 0843.

[29] A. L. Cabrera, F. Vargas and R. A. Zarate, *J. Phys. Chem. Solids*, 1994, 55, 1303-1307.

[30] A. L. Cabrera, G. Tarrach, P. Lagos and G. B. Cabrera, *Ferroelectrics*, 2002, 281, 53-66.

[31] A.-C. Iancu, G. A. Lungu, C. A. Tache and C. M. Teodorescu, *Mater. Adv.*, 2024, 5, 8798-8811.

[32] S. Banerjee and V. R. Choudhary, *J. Chem. Sci.*, 2000, 112, 535-542.

[33] T. Watanabe and T. Ohba, *ACS Sustain. Chem. Eng.*, 2021, 9, 3860-3873.

[34] C. Hwang, O. Gwon, H. Jo, K. M. Ok and G. Kim, *ChemElectroChem*, 2017, 4, 468-471.

[35] P. V. Gosavi and R. B. Biniwale, *Mater. Chem. Phys.*, 2010, 119, 324-329.

[36] P. Porta, S. De Rossi, M. Faticanti, G. Minelli, I. Pettiti, L. Lisi and M. Turco, *J. Solid State Chem.*, 1999, 146, 291-304.

[37] H. Arandiyan, S. S. Mofarah, C. C. Sorrell, E. Doustkhah, B. Sajjadi, D. Hao, Y. Wang, H. Sun, B.-J. Ni, M. Rezaei, Z. Shao and T. Maschmeyer, *Chem. Soc. Rev.*, 2021, 50, 10116-10211.

[38] T. Watanabe, S. M. Khan, H. Kanoh and T. Ohba, *Phys. Chem. Ind. J.*, 2017, S1, 101-109.

[39] G. Valderrama, C. Urbina de Navarro and M. R. Goldwasser, *J. Power Sources*, 2013, 234, 31-37.

[40] B. J. Hare, D. Maiti, A. J. Meier, V. R. Bhethanabotla and J. N. Kuhn, *Ind. Eng. Chem. Res.*, 2019, 58, 12551-12560.

[41] F. Li, H. Zhan, N. Zhao and F. Xiao, *Int. J. Hydrog. Energy*, 2017, 42, 20649-20657.

[42] Q. Wang, Y. Xuan, Z. Zhu, L. Teng, X. Liu and Y. Gao, *J. Mater. Chem. A*, 2025, 13, 29558-29569.

[43] Mahesh M. Nair and S. Abanades, *Sustainable Energy Fuels*, 2018, 2, 843-854.

[44] T. Watanabe and T. Ohba, *Nanoscale*, 2022, 14, 8318-8325.

[45] K. V. Sopiha, O. I. Malyi, C. Persson and P. Wu, *Phys. Chem. Chem. Phys.*, 2018, 20, 18828-18836.

[46] J. M. D. Tascón and L. G. Tejuca, *J. Chem. Soc. Faraday Trans. 1*, 1981, 77, 591-602.

[47] R. Hammami, H. Batis and C. Minot, *Surf. Sci.*, 2009, 603, 3057-3067.

[48] J. M. Polfus, B. Yildiz, H. L. Tuller and R. Bredesen, *J. Phys. Chem. C*, 2018, 122, 307-314.

[49] Q. Yang and Y. S. Lin, *Ind. Eng. Chem. Res.*, 2006, 45, 6302-6310.

[50] Y. S. Lin, Q. Yang and J. Ida, *J. Taiwan Inst. Chem. Eng.*, 2009, 40, 276-280.

[51] Q. Zheng, L. Huang, Z. Zhong, B. Louis and Q. Wang, *Chem. Eng. J.*, 2020, 380, 122444.

[52] T. Ohba, Y. Ohyama and H. Kanoh, *RSC Adv.*, 2014, 4, 32647-32650.

[53] D. Hoshi, T. Watanabe and T. Ohba, *TANSO*, 2017, 2017,

198-202.

[54] S. Wada, H. Yasuno, T. Hoshina, S.-M. Nam, H. Kakemoto and T. Tsurumi, Japanese *J. Appl. Phys.*, 2003, 42, 6188.

[55] T. Yan, Z.-G. Shen, W.-W. Zhang and J.-F. Chen, *Mater. Chem. Phys.*, 2006, 98, 450-455.

[56] Y. Goto, K. Yamazaki, M. Kikugawa and M. Aoki, *Dalton Trans.*, 2024, 53, 13847-13853.

[57] Y. A. Daza, R. A. Kent, M. M. Yung and J. N. Kuhn, *Ind. Eng. Chem. Res.*, 2014, 53, 5828-5837.

[58] K. Kang, H. Sampei and Y. Sekine, *RSC Sustain.*, 2025, 3, 1598-1628.

[59] L. Lindenthal, J. Popovic, R. Rameshan, J. Huber, F. Schrenk, T. Ruh, A. Nenning, S. Löffler, A. K. Opitz and C. Rameshan, *Appl. Catal. B*, 2021, 292, 120183.

[60] Y. Nishihata, J. Mizuki, T. Akao, H. Tanaka, M. Uenishi, M. Kimura, T. Okamoto and N. Hamada, *Nature*, 2002, 418, 164-167.

[61] D. Neagu, G. Tsekouras, D. N. Miller, H. Ménard and J. T. S. Irvine, *Nat. Chem.*, 2013, 5, 916-923.

[62] F. J. Pomiro, G. G. Fouga, A. E. Bohé, J. E. Gayone and G. De Micco, *J. Environ. Chem. Eng.*, 2024, 12, 112317.

[63] A. Akhtar, A. Zaidi, C. de Leeuwe, A. M. Efstathiou, A. Asghar, M. G. Hassan-Sayed and S. Z. Abbas, *J. Environ. Chem. Eng.*, 2025, 13, 119640.

[64] H. J. Muñoz, S. A. Korili and A. Gil, *Catal. Rev. - Sci. Eng.*, 2026, 68, 91-143.

[65] G. Valderrama, M. R. Goldwasser, C. U. d. Navarro, J. M. Tatibouët, J. Barrault, C. Batiot-Dupeyrat and F. Martínez, *Catal. Today*, 2005, 107-108, 785-791.

[66] S. Li and S. Haussener, *Appl. Energy*, 2023, 334, 120617.

[67] Y. Zhao, W. Gao, S. Li, G. R. Williams, A. H. Mahadi and D. Ma, *Joule*, 2019, 3, 920-937.

[68] Y. Kim, H. S. Kim, H. Kim, J. Ha, D. Kang and J. W. Lee, *Korean J. Chem. Eng.*, 2025, 42, 3081-3100.

[69] J. E. Miller, A. H. McDaniel and M. D. Allendorf, *Adv. Energy Mater.*, 2014, 4, 1300469.

[70] M. Lee, Y. Kim, H. S. Lim, A. Jo, D. Kang and J. W. Lee, *Energies*, 2020, 13, 5324.

[71] Z. Xiao, H. Zhang, X. Tan, F. Ye, Y. Zhang, J. Gu, J. Li, K. Sun, S. Zhang, J.-J. Zou and D. Wang, *Adv. Energy Mater.*, 2025, 15, 2500988.

[72] S. Zeng, P. Kar, U. K. Thakur and K. Shankar, *Nanotechnology*, 2018, 29, 052001.

[73] R. Thalinger, A. K. Opitz, S. Kogler, M. Heggen, D. Stroppa, D. Schmidmair, R. Tappert, J. Fleig, B. Klötzer and S. Penner, *J. Phys. Chem. C*, 2015, 119, 11739-11753.

[74] M. Cai, Z. Wu, Z. Li, L. Wang, W. Sun, A. A. Tountas, C. Li, S. Wang, K. Feng, A.-B. Xu, S. Tang, A. Tavasoli, M. Peng, W. Liu, A. S. Helmy, L. He, G. A. Ozin and X. Zhang, *Nat. Energy*, 2021, 6, 807-814.

[75] E. Delikonstantis, M. Scapinello, V. Singh, H. Poelman, C. Montesano, L. M. Martini, P. Tosi, G. B. Marin, K. M. Van Geem, V. V. Galvita and G. D. Stefanidis, *ACS Energy Lett.*, 2022, 7, 1896-1902.

[76] J. Chen, S. Su, C. Wang, Q. Li, H. Wang, W. Xu, X. Li and H. Jia, *Chem. Eng. J.*, 2023, 476, 146712.

[77] L. Liu, S. Das, T. Chen, N. Dewangan, J. Ashok, S. Xi, A. Borgna, Z. Li and S. Kawi, *Appl. Catal. B*, 2020, 265, 118573.

[78] W. Wang, M. Nguyen-Quang, D. Mateo, X. Yong, T. Li, H. Xie, W. Chu, C. Pham-Huu, X. Tu and J. Gascon, *ACS Catal.*, 2025, 15, 10868-10896.

[79] M. Barreau, D. Salusso, J. Zhang, M. Haevecker, D. Teschner, A. Efimenko, F. Bournel, J.-J. Gallet, E. Borfecchia, K. Sobczak, C. Petit and S. Zafeiratos, *J. Mater. Chem. A*, 2024, 12, 7605-7621.

[80] A. A. Alkhoori, E. P. Komarala, A. A. Dabbawala, A. G. S. Hussien, D. H. Anjum, S. Mao and K. Polychronopoulou, *RSC Sustain.*, 2024, 2, 3866-3878.

[81] F. Schrenk, L. Lindenthal, G. Pacholik, T. Navratil, T. M. Berger, H. Drexler, R. Rameshan, T. Ruh, K. Föttinger and C. Rameshan, *Compounds*, 2022, 2, 378.

[82] A. J. Poerjoto, J. Ashok, N. Dewangan and S. Kawi, *J. CO2 Util.*, 2021, 47, 101498.

[83] T. Wang, M. Su, Q. Wang and Z. Li, *Energy Technol.*, 2023, 11, 2300180.

[84] H. Nazir, C. Louis, S. Jose, J. Prakash, N. Muthuswamy, M. E. M. Buan, C. Flox, S. Chavan, X. Shi, P. Kauranen, T. Kallio, G. Maia, K. Tammeveski, N. Lymperopoulos, E. Carcadea, E. Veziroglu, A. Iranzo and A. M. Kannan, *Int. J. Hydrog. Energy*, 2020, 45, 13777-13788.

[85] L. Wang, T. Ma, S. Dai, T. Ren, Z. Chang, L. Dou, M. Fu and X. Li, *Chem. Eng. J.*, 2020, 389, 124426.

[86] J. Zhang, V. Haribal and F. Li, *Sci. Adv.*, 3, e1701184.

[87] H. Notohara, K. Urita and I. Moriguchi, *ACS Appl. Mater. Interfaces*, 2023, 15, 30600-30605.

[88] K. Urita, Y. Shiga, T. Fujimori, T. Iiyama, Y. Hattori, H. Kanoh, T. Ohba, H. Tanaka, M. Yudasaka, S. Iijima, I. Moriguchi, F. Okino, M. Endo and K. Kaneko, *J. Am. Chem. Soc.*, 2011, 133, 10344-10347.

[89] S. Takawane, M. Miyamoto, T. Watanabe and T. Ohba, *RSC Sustain.*, 2024, 2, 2218-2224.